



## X-ray computed tomography of gas diffusion layers of PEM fuel cells: Segmentation of the microporous layer

Andreas Pfrang <sup>a,\*</sup>, Stephan Didas <sup>b</sup>, Georgios Tsotridis <sup>a</sup>

<sup>a</sup> Institute for Energy and Transport, Joint Research Centre, European Commission, NL-1755 ZG Petten, The Netherlands

<sup>b</sup> Fachhochschule Trier, Umwelt-Campus Birkenfeld, Postfach 1380, D-55761 Birkenfeld, Germany

### HIGHLIGHTS

- Gas diffusion layers for PEMFC were examined by X-ray computed tomography.
- Advanced segmentation algorithms were applied for the discrimination of materials.
- The 3D distribution of the material of the microporous layer was determined.

### ARTICLE INFO

#### Article history:

Received 1 August 2012

Received in revised form

11 December 2012

Accepted 30 January 2013

Available online 13 February 2013

#### Keywords:

Proton exchange membrane fuel cell

Gas diffusion layer

Microporous layer

X-ray computed tomography

Segmentation

### ABSTRACT

In proton exchange membrane fuel cells (PEMFCs), gas diffusion layers (GDL) are crucial for fuel cell performance and more specifically for the removal of the product water where the microporous layer (MPL), as one component of the GDL, plays a significant rule.

X-ray computed tomography was applied for the 3D imaging of a gas diffusion layer – Sigracet GDL 35 BC – at sub- $\mu$ m resolution to improve the knowledge of its 3D microstructure. The study was focused on the identification of the MPL material within the GDL. A segmentation based on a simple gray level thresholding is not appropriate as the gray level ranges for air, carbon fibres and MPL overlap. Consequently, more sophisticated approaches for segmentation were tested; diffusion filtering followed by a gray level thresholding gave the best results. Using this approach, fractures in the MPL layer could be visualised and it was also shown that the MPL can penetrate far into the GDL.

© 2013 Elsevier B.V. All rights reserved.

## 1. Introduction

While fuel cells in general are expected to play a significant role in the future energy applications, proton exchange membrane (PEM) fuel cells can potentially play an important role for automotive applications due to their fast start-up and flexibility in power output as compared to other fuel cell technologies [1].

In a proton exchange membrane fuel cell (PEMFC), the membrane-electrode assembly (MEA) forms the functional core which includes two gas diffusion layers (GDL). Each of these GDLs has to fulfil multiple functions: to provide gas access from the flow field channels of the bipolar plate to the catalyst layer, to allow the removal of the product water, to mechanically stabilize the membrane-electrode assembly, and finally to provide electronic and thermal conductivity between catalyst layer and bipolar plate.

The GDL typically consists of carbon fibre papers or felts which are impregnated with polytetrafluoroethylene (PTFE) to achieve a partial hydrophobization of the surfaces [2]. Often a microporous layer (MPL) which consists of a mixture of carbon black and PTFE is applied on the side facing the catalyst layer for a further optimization of the water management [2–4].

While scanning electron microscopy is still a standard technique for the characterization of GDLs and MEAs [2], improvement in instrumentation in the recent years allowed the imaging of gas diffusion layers at resolutions below 1  $\mu$ m by synchrotron-based tomography [5–7] as well as X-ray computed tomography [8–11] whereby also MPL material was investigated [12,13]. For a better understanding of water management, operating fuel cells have been imaged by synchrotron-based methods and soft X-ray radiography e.g. for imaging of liquid water in the GDL [14–17].

In this paper, the segmentation of the different components in an X-ray computed tomography dataset of a GDL is discussed. It is demonstrated that MPL material can be discriminated from carbon fibres and PTFE applying advanced segmentation techniques.

\* Corresponding author. Tel.: +31 224 565047; fax: +31 224 565623.

E-mail address: [andreas.pfrang@ec.europa.eu](mailto:andreas.pfrang@ec.europa.eu) (A. Pfrang).

## 2. Experimental

### 2.1. Materials

A carbon fibre based gas diffusion layer equipped with microporous layer (MPL) was investigated: the carbon paper Sigracet GDL 35 BC (SGL Group, Wiesbaden, Germany). **Table 1** summarizes some of the sample properties as given by the manufacturer.

### 2.2. Scanning electron microscopy (SEM)

A Zeiss Supra 50 FEG scanning electron microscope (SEM) was used to image the gas diffusion layers from both, the MPL treated side and the back side.

### 2.3. X-ray computed tomography (CT)

Strips with a width of about 3 mm and a length of about 10 mm were cut from the gas diffusion layer. These strips were investigated using a ‘nanotom® s’ computed tomography system (GE Sensing & Inspection Technologies, phoenix x-ray, Wunstorf, Germany). This system includes a 180 kV x-ray tube and a 2D x-ray detector with  $2300 \times 2300$  pixels.

X-rays with a maximum energy of 52 keV were used for imaging and no filter was inserted into the beam path. 900 X-ray projections at different orientation of the sample were acquired. Each projection was generated by integration of four images with an integration time of 2000 ms each. Based on these projections, the volume was reconstructed by filtered backprojection. Voxel size was  $0.8 \mu\text{m}$  which is close to the maximum resolution of ca.  $1.0 \mu\text{m}$  that can be achieved with this tomography system. The investigated field of view was about  $800 \mu\text{m} \times 650 \mu\text{m} \times 500 \mu\text{m}$ .

### 2.4. Data processing

The reconstructed X-ray CT data was imported into MAVI V1.4 (Modular Algorithms for Volume Images by Fraunhofer ITWM, Kaiserlautern, Germany [19]) and processed further. The data was prepared by spreading the gray values over the whole 16 bit gray value range.

## 3. Results and discussion

**Fig. 1** shows top-view scanning electron micrographs of both sides of the GDL as received. On the left image (side facing the bipolar plate), carbon fibres and PTFE are clearly visible. The range of diameters of the carbon fibres determined by SEM is 6–7  $\mu\text{m}$ .

The right image of the side facing the catalyst layer shows MPL material as well as a crack in the MPL material. The inset shows a high resolution scanning electron micrograph of MPL particles with typical dimensions well below 100 nm.

The SEM offers a resolution down to the nm scale, but the acquisition of scanning electron micrographs of the internal structure of gas diffusion layers is more demanding as a cross-section of the GDL has to be prepared.

X-ray computed tomography allows the non-destructive acquisition of 3D images of the GDL’s microstructure. The SEM top views of **Fig. 1** show that e.g. for the determination of the 3D

distribution of MPL material and cracks in the MPL material, CT will potentially provide additional insight. But even though carbon fibres are clearly visible in the original CT data (see top images of **Fig. 5**), a discrimination of all three components of the GDL – namely carbon fibres, PTFE and MPL – and air is not straight forward.

**Fig. 2** shows the gray value distribution of the original CT dataset after spreading the gray values over the whole gray value range. Only one peak is visible and this peak exhibits one shoulder to the right (marked by an arrow in **Fig. 2**) which suggests the presence of at least a second phase. Consequently it is reasonable to try to discriminate at least two phases using binarization based on a gray level threshold.

### 3.1. Identification of carbon fibres (incl. PTFE)

A mean filter was applied to the whole image. Afterwards for segmentation, a certain gray value threshold was chosen to generate a 3D model from the gray valued 3D dataset. Voxels brighter than this global threshold were assigned to carbon fibres (incl. PTFE), voxels darker than this threshold gray-value contain either air or MPL material. It should be noted that carbon fibres and PTFE material could not be discriminated, i.e. the resulting 3D model contains carbon fibres and PTFE (see **Fig. 3**).

As – due to noise in the raw data – small particles were found in the 3D model that do not correspond to the real structure, they were removed by labelling particles and then applying object filtering to remove particles that are small relative to the carbon fibres.

As the filling factor strongly depends on the selected gray level threshold [11], the porosity is compared with manufacturer’s data (see **Table 1**) of 90% at a nominal thickness of 0.30 mm as first check for the segmentation of the fibres. Considering a volume with this nominal thickness of 0.30 mm, the filling factor is 8.3%, which is in reasonable agreement with manufacturer’s data. Further, the continuity of the fibres as well as the general morphology in the resulting 3D model is checked. Finally, the average fibre diameter of the resulting 3D model is estimated by applying spherical granulometry and compared with SEM measurements. The spherical granulometry assigns to each voxel of an identified phase – in this case the fibre incl. PTFE are considered – the diameter of the largest sphere which is completely contained in the identified phase and covering the pixel. It thus yields the local structure thickness which for ideal fibres corresponds to the fibre diameter. The peak of the 2D Gaussian fit of the corresponding curve of number of voxels vs. local structure thickness is at 6.4  $\mu\text{m}$  which corresponds well with the range of fibre diameters of 6–7  $\mu\text{m}$  determined from SEM images.

In a second segmentation step, MPL material and air were separated. As attempts based on a simple global thresholding were not successful due to the overlap of gray values of MPL and air, two alternative approaches – based on hysteresis binarization and diffusion filtering, respectively – were applied.

### 3.2. Identification of the MPL using hysteresis binarization

A mean filter was applied to the whole image. Then the complement of the 3D image of fibres and PTFE was used to mask the

**Table 1**

Properties of the investigated GDL as given by the manufacturer [18].

Sample	Microporous layer (MPL)	Thickness/mm	PTFE/wt%	Porosity (incl. PTFE)/%	Area density (incl. PTFE)/g $\text{cm}^{-2}$
Sigracet 35 BC	Yes	0.325 (0.30 without MPL)	5	80 (90 without MPL)	110 (54 without MPL)

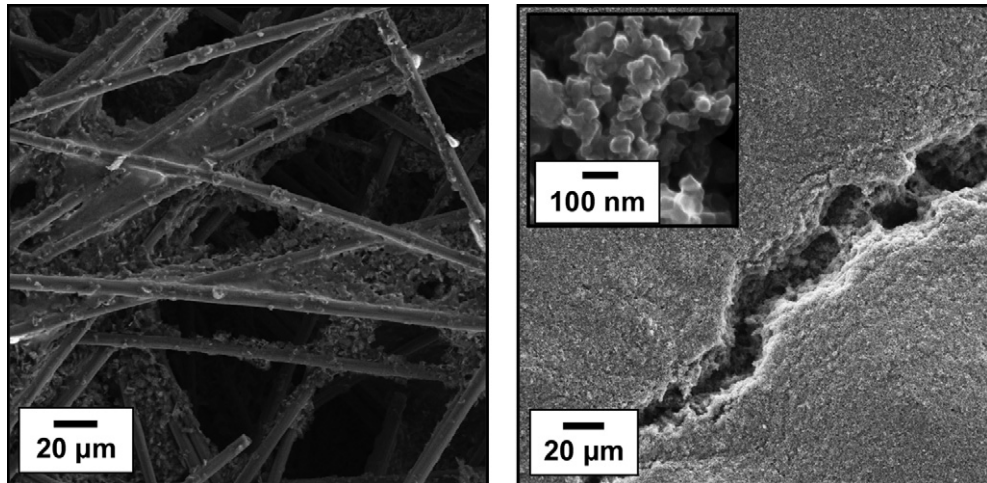


**Fig. 1.** Scanning Electron Micrographs of the SGL GDL 35BC. Left) Top-view of the side oriented to the bipolar plate, right) MPL side; the inset shows a high resolution SEM image of the MPL particles.

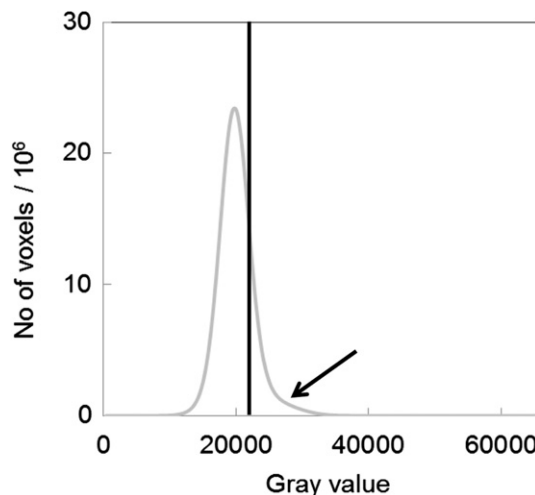


**Fig. 2.** Gray value distribution of voxels in the original CT dataset. The arrow marks a shoulder of the main peak which suggests at least two different phases (for an evaluation after segmentation see Fig. 7). The black line marks the global threshold used for the segmentation of carbon fibres (incl PTFE).

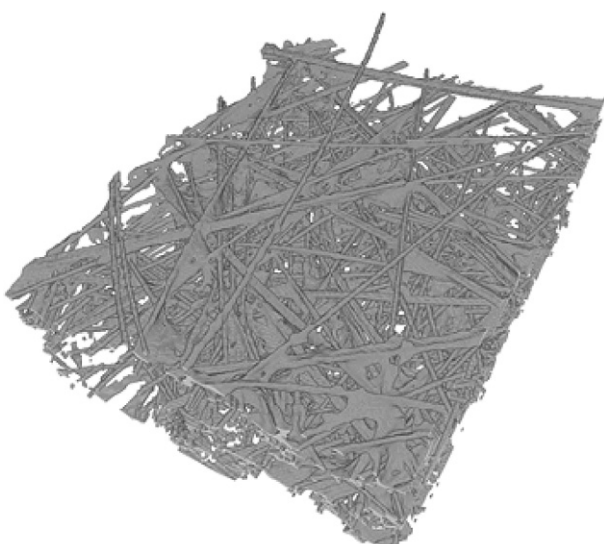


**Fig. 3.** 3D visualization of fibres and PTFE in SGL GDL 35 BC.

dataset. On these remaining voxels, a hysteresis thresholding was carried out.

This function transformed the original gray scale image into a black and white image by a two-step procedure with the input of one high and one low threshold value. First, a simple global thresholding using the higher threshold is applied assigning voxels above the threshold to MPL material. Subsequently, for each voxel neighbouring a voxel assigned to MPL material, it is checked whether its gray value exceeds the second (lower) threshold. The neighbouring voxel is assigned to the MPL if this condition is fulfilled and to air otherwise. This is repeated as long as the MPL phase still grows. This process is also referred to as double thresholding and yields smooth connected foreground components without emphasizing noise [19].

This step is followed by a morphological closure, i.e. dilation followed by erosion. Closure was used to remove small holes or to connect interrupted objects within the MPL phase while keeping the remainder of the image unchanged.

As fibres are often surrounded by a darker sheath in the original dataset (see Fig. 4) due to phase contrast effects at the transition

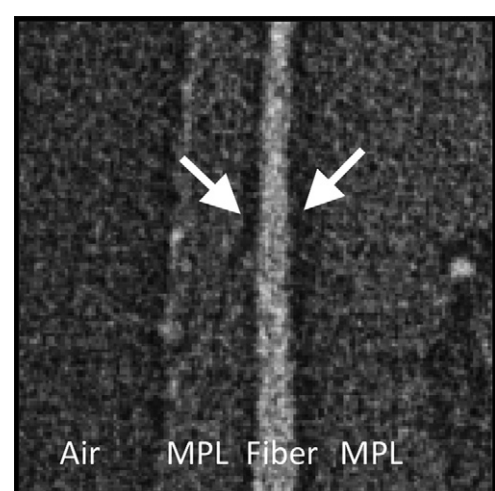


**Fig. 4.** Cross-section of the original CT dataset of SGL GDL 35BC showing one fibre embedded in the MPL. Dark lines are observed next to carbon fibres (marked by white arrows).

between different materials, gaps between fibres and MPL still had to be closed.

For this purpose, the Euclidian distance transform of the current MPL image was calculated, i.e. each voxel not belonging to the MPL was assigned the closest distance to an MPL voxel. Then the Euclidian distance transform of the image of fibres and PTFE was calculated. Both resulting datasets were added and then

global thresholding was carried out to select voxels with a low distance to MPL and fibres (incl. PTFE). The result was then masked with the complement of the MPL image and the complement of the image of fibres and PTFE and added to the original MPL image. Fig. 5, middle, shows cross-sections of the final image of MPL and fibres (incl. PTFE) without artificial gaps between MPL and fibres.

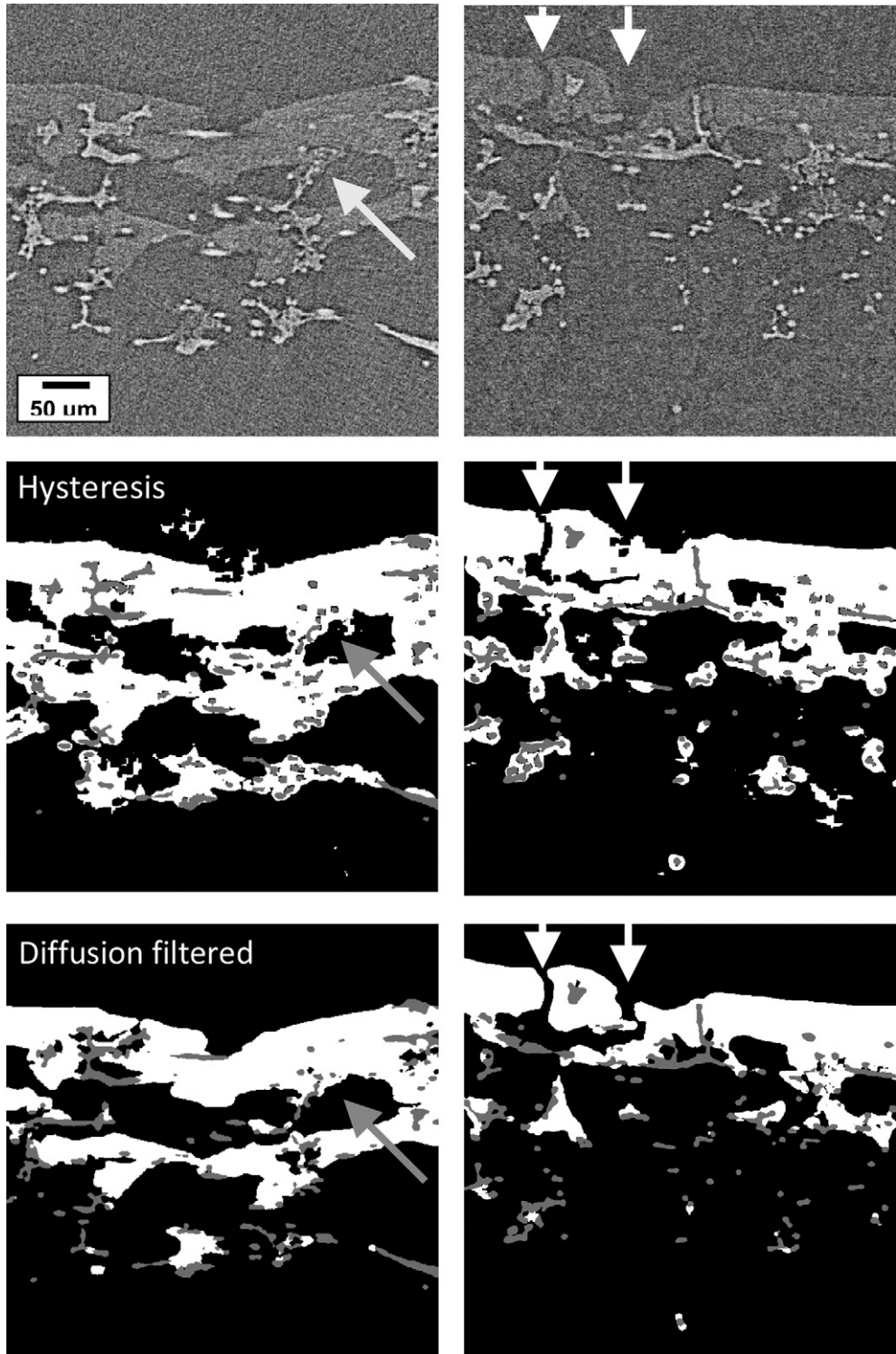


**Fig. 5.** Cross-sections of the GDL: top) original CT dataset, middle) after segmentation applying hysteresis binarization, bottom) after segmentation applying diffusion filtering. For the latter two, the fibres are shown in dark gray; the MPL is shown in white. Left and right show two different cross-sections which are perpendicular with respect to each other and at the same time perpendicular to the GDL layer. The gray arrows on the left mark a void in the MPL layer; the white arrows on the right mark cracks in the MPL layer.

### 3.3. Identification of the MPL using diffusion filtering

To simplify the image data and remove noise, nonlinear isotropic diffusion filtering has been applied as a first step. We have used a Perona–Malik model to process the data [20,21]. The idea of this model is to understand an image as temperature distribution in the image domain. The initial image data gives the temperature distribution at the starting time. Solving the nonlinear diffusion equation simulates the temperature distribution at later times if no external heat sources are present. Image regions with high contrast are modelled as parts of the material with low diffusion coefficient. To cope with the large amount of data, an implementation based on additive operator splitting (AOS) has been chosen [22]. Concerning the choice of the parameters, one has to make sure that the scale parameter  $\lambda$  has to be chosen with respect to the order of magnitude of the measurements, i.e. in the range of  $10^3$ . This first step allows removing noise from the image data in order to segment the image with a simple thresholding method.

On this filtered dataset a global thresholding was applied leading to an approximate discrimination of air and all solid material (i.e. fibres, PTFE and MPL). Due to the diffusion filtering, the fibres had got a larger – too large – diameter.

In the next step these fibres and PTFE were removed: The Euclidian distance transform of the image containing fibres and PTFE (see 'Identification of carbon fibres (incl. PTFE)') was calculated and a global threshold was used to generate an image containing fibres (incl. PTFE) plus a layer of a certain thickness corresponding to the growth in diameter due to diffusion filtering. This image was complemented and used as mask on the diffusion filtered image.

Then, small particles still present in the masked image that did not correspond to the real MPL structure were removed by labelling all particles and then applying object filtering.

Finally, the gap between MPL and fibres (incl. PTFE) generated by earlier step where fibres and PTFE were removed, had to be closed again. Again – as used for the identification of the MPL by hysteresis segmentation – the Euclidian distance transforms of the current MPL image and of the image of fibres and PTFE were calculated, added, and global thresholding was carried out on the sum to select voxels with a with low distance to MPL and fibres (incl. PTFE). The result was then masked with the complement of the MPL image and the complement of the image of fibres and PTFE and added to the original MPL image. Fig. 5, bottom, shows cross-sections of the final image of MPL (white) and fibres and PTFE (gray). Fig. 6 shows a 3D reconstruction of the same dataset.

Fig. 5 shows exemplary two cross-sections of SGL GDL BC35, where the bottom side of the GDL would be oriented towards the bipolar plate. The top images show original CT data after reconstruction: the carbon fibres are clearly visible and also MPL material can be detected, even though the ranges of gray levels of MPL and air overlap strongly.

The middle images of Fig. 5 show the same cross-sections after segmentation applying hysteresis binarization. Even though the two thresholds for segmentation were optimized, a perfect identification of MPL material could not be achieved. The bulk MPL material was correctly determined, but especially at boundaries to other phases – i.e. air or carbon fibres – often too much volume is assigned to MPL material. Considering for example the right cross-section (applying hysteresis binarization), one fracture (marked by the right white arrow) is not represented properly and also fibres artificially are coated by MPL material (see e.g. fibres in the bottom center in the right cross-section after hysteresis binarization).

The bottom images of Fig. 5 show the same cross-sections after segmentation applying diffusion filtering. Here, the void in the MPL layer is represented correctly (see gray arrow in left bottom image), cracks are clearly visible (see white arrows in right bottom image) and no obvious artificial coating of fibres with MPL material is observed.

Comparing the segmentation based on hysteresis binarization and diffusion filtering, it is obvious that a better agreement with the original data was achieved using diffusion filtering. The corresponding 3D reconstruction is shown in Fig. 6. As also in the left cross-section of Fig. 5, a void in the MPL was observed.

This void extends over a significant fraction of the investigated volume and is therefore also clearly visible in the plot in Fig. 6 on the right, where the filling factors for MPL, fibres (incl. PTFE) and the overall filling factor are plotted against the location within the cross-section of the GDL, where the plotted 325  $\mu\text{m}$  correspond to the nominal thickness of the GDL (see Table 1). The void in the MPL material results in a local minimum of the filling factor of MPL material at a thickness of about 150  $\mu\text{m}$ .

Further it is also clearly visible that the highest density of MPL material is found close to the side of the GDL facing the electrode with a maximum volume fraction of about 80% at a distance of about 80  $\mu\text{m}$  to the GDL surface.

When comparing the results presented here with a study by Fishman and Bazylak [12] where the MPL distribution in SGL 35 BC was also determined using X-ray computed tomography but using a different approach for segmentation, it should be considered that

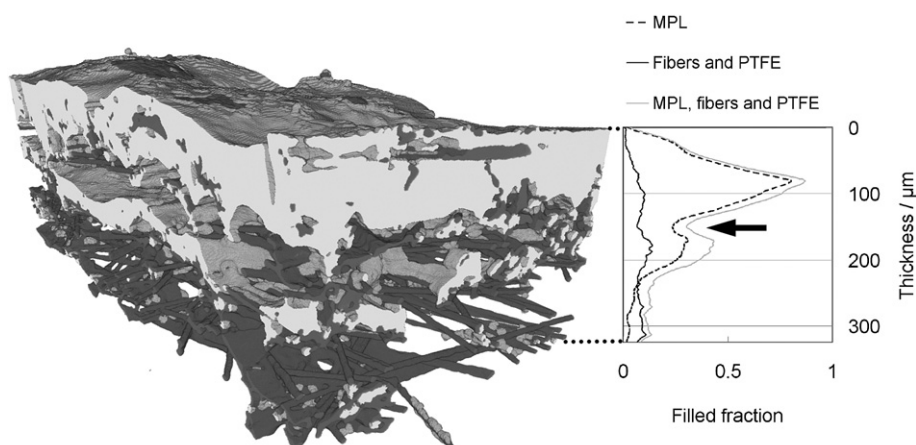


**Fig. 6.** 3D reconstruction of the GDL on the left: the fibres are shown in dark gray; the MPL is shown in bright gray. On the right, the filling factors for MPL, fibres and PTFE and overall filling factor (containing MPL, fibres and PTFE) are plotted vs. the distance from the surface of the GDL cathode side.

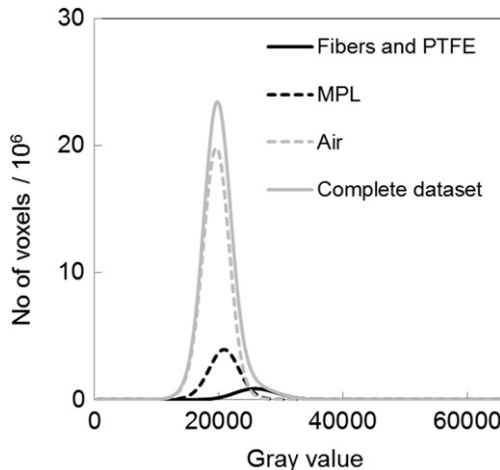


Fig. 7. Gray value distribution of voxels in the original CT dataset.

the authors suggest that a fraction of carbon fibres and PTFE could be erroneously assigned to MPL material. In this context, a maximum MPL filling factor of about 80% found here seems to agree to the minimum porosity with respect to MPL of 15% given in Ref. [12]. They observed a 'distinct step' in MPL porosity near the middle of the GDL and while they interpret this as a 'significant collection of residual MPL material', in the current study a clear minimum in MPL filling factor was observed near the center of the GDL (see arrow in Fig. 6) which is followed by a second maximum in MP filling factor when moving towards the bipolar plate side. The minimum corresponds to a void in the MPL which is clearly visible in Figs. 5 and 6. The two local porosity minima of fibres found in Ref. [12], are also visible in Fig. 6 even though much less pronounced and not at the same depths. Overall, the results of both investigations agree and the slight differences could be attributed to differences in segmentation algorithms as well as possibly statistical variation of GDL structure from location to location and from batch to batch.

Fig. 7 shows the gray value distribution of voxels in the original CT dataset including the gray value distribution for each of the segmented phases (i.e. air, MPL and fibres incl. PTFE) based on segmentation applying diffusion filtering. Even though the fibres (incl. PTFE) show a significantly higher average gray value than MPL or air, the gray value distribution of fibres (incl. PTFE) overlaps with both, the gray value distributions for air and MPL.

Even though the average gray value of MPL voxels is clearly higher than the average gray value of air voxels, the gray value distributions for air and MPL overlap very strongly. More specifically, the distribution for MPL voxels – covering a smaller range of gray values than the one for air – is almost completely contained in the range of gray values for air.

#### 4. Conclusions

X-ray computed tomography was applied for the 3D imaging of a Sigracet GDL 35 BC gas diffusion layer at sub- $\mu\text{m}$  resolution. Main goal of the investigation was the identification of MPL material within the GDL.

In a first step of the evaluation of the CT data, a segmentation based on a simple gray level thresholding was applied to separate air and MPL material on one side from carbon fibres and PTFE on the other side.

As the gray level ranges for air and MPL overlap, more sophisticated approaches for segmentation were tested: one approach

based on hysteresis segmentation and a second approach based on diffusion filtering followed by a simple gray level thresholding. The latter gave the best results: fractures in the MPL layer could be visualised and it was also shown that the MPL can penetrate far into the GDL.

Overall, it was demonstrated that – even for a severe overlap of gray values of different materials in the CT data of a GDL – it is possible to discriminate air, MPL material and carbon fibres. This improved evaluation of CT data is crucial for a better understanding of the 3D microstructure of a GDL and therefore for a better understanding of its performance.

#### Acknowledgements

This work has been carried out within the multi-year program of the European Commission's Joint Research Centre under the auspices of the FCPOINT action. The authors would like to thank GE Sensing & Inspection Technologies, phoenix x-ray (Wunstorf, Germany) for CT measurements, Marijke Roos and Gaby Janssen (ECN) for provision of samples and fruitful discussions, and Marc Steen for critical reading of the manuscript.

#### References

- [1] I. Cerri, F. Lefebvre-Joud, P. Holtappels, K. Honegger, T. Stubos, P. Millet, A. Pfrang, M. Bielewski, E. Tzimas, Scientific Assessment in Support of the Materials Roadmap Enabling Low Carbon Energy Technologies: Hydrogen and Fuel Cells, Publications Office of the European Union, Luxembourg, 2012, ISBN 978-92-79-23911-3.
- [2] M.F. Mathias, J. Roth, J. Fleming, W. Lehnert, Diffusion media materials and characterisation, in: Handbook of Fuel Cells – Fundamentals, Technology and Applications, vol. 3, John Wiley, Chichester, 2003, pp. 517–537.
- [3] L. Giorgi, E. Antolini, A. Pozio, E. Passalacqua, *Electrochimica Acta* 43 (24) (1998) 3675–3680.
- [4] V.A. Paganin, E.A. Ticianelli, E.R. Gonzalez, *Journal of Applied Electrochemistry* 26 (3) (1996) 297–304.
- [5] J. Becker, V. Schulz, A. Wiegmann, *Journal of Fuel Cell Science and Technology* 5 (2) (2008), art. no. 021006.
- [6] J. Becker, R. Flückiger, M. Reum, F.N. Büchi, F. Marone, M. Stampanoni, *Journal of the Electrochemical Society* 156 (10) (2009) B1175–B1181.
- [7] I. Manke, C. Hartnig, N. Kardjilov, H. Riesemeier, J. Goebels, R. Kuhn, P. Krüger, J. Banhart, *Fuel Cells* 10 (1) (2010) 26–34.
- [8] H. Ostadi, K. Jiang, P.D. Prewett, *Micro and Nano Letters* 3 (4) (2008) 106–109.
- [9] A. Pfrang, D. Veyret, F. Sieker, G. Tsotridis, *International Journal of Hydrogen Energy* 35 (8) (2010) 3751–3757.
- [10] A. Pfrang, D. Veyret, G.J.M. Janssen, G. Tsotridis, *Journal of Power Sources* 196 (12) (2011) 5272–5276.
- [11] H. Ostadi, P. Rama, Y. Liu, R. Chen, X.X. Zhang, K. Jiang, *Chemical Engineering Science* 65 (6) (2010) 2213–2217.
- [12] Z. Fishman, A. Bazylak, *Journal of the Electrochemical Society* 158 (8) (2011) B846–B851.
- [13] A. Pfrang, D. Veyret, G. Tsotridis, Computation of thermal conductivity of gas diffusion layers of PEM fuel cells, in: A. Ahsan (Ed.), *Convection and Conduction Heat Transfer*, Intech, 2011.
- [14] P.K. Sinha, P. Halleck, C.Y. Wang, *Electrochemical and Solid-State Letters* 9 (7) (2006) A344–A348.
- [15] A. Bazylak, *International Journal of Hydrogen Energy* 34 (9) (2009) 3845–3857.
- [16] S. Tsushima, S. Hirai, *Progress in Energy and Combustion Science* 37 (2) (2011) 204–220.
- [17] T. Sasabe, S. Tsushima, S. Hirai, *International Journal of Hydrogen Energy* 35 (20) (2010) 11119–11128.
- [18] Sigracet, 34 & 35 Series Gas Diffusion Layer – Manufacturer Data Sheet, SGL Group, Wiesbaden, Germany, 2007.
- [19] Modular Algorithms for Volume Imaging (MAVI), Homepage of the MAVI Software, Fraunhofer ITWM, Kaiserslautern, Germany, 2011.
- [20] P. Perona, I. Malik, *IEEE Transactions on Pattern Analysis and Machine Intelligence* 12 (7) (1990) 629–639.
- [21] J. Weickert, A review of nonlinear diffusion filtering, in: B. ter Haar Romeny (Ed.), *Scale-space Theory in Computer Vision*, LNCS, vol. 1252, Springer, 1997, pp. 1–28.
- [22] J. Weickert, B.M. ter Haar Romeny, M.A. Viergever, *IEEE Transactions on Image Processing* 7 (3) (1998) 398–410.